

Two-dimensional imaging of metastable CO molecules

Rienk T. Jongma, Theo Rasing, and Gerard Meijer

Research Institute for Materials, University of Nijmegen Toernooiveld, 6525 ED, Nijmegen, The Netherlands

(Received 16 August 1994; accepted 20 October 1994)

Direct time and spatially resolved detection of metastable CO molecules, prepared in selected quantum states via pulsed laser excitation, is experimentally demonstrated in a molecular beam machine. Characterization of the molecular beam in terms of parallel and perpendicular velocity distributions and rotational temperatures is performed. A direct two-dimensional (2D) demonstration of the mass-focusing effect in binary gas mixtures is given. Two-dimensional imaging of the spatial distribution of the metastable $a^3\Pi$ CO molecules in the beam after passage through a hexapole field is used to study hexapole focusing performance. Structured 2D images demonstrate the dependence of the focusing characteristics on the magnitude of the Λ -doubling and on the angular dependence of the focusing force in a hexapole consisting of cylindrical rods. © 1995 American Institute of Physics.

I. INTRODUCTION

Over the last few years a variety of two-dimensional (2D) imaging techniques have been experimentally demonstrated and applied in different fields. Spatially resolved detection of planar laser induced fluorescence has turned out to be a powerful tool in combustion diagnostics and has been used for *in situ* 2D visualization of combustion species not only in stationary flames but also in combustion chambers of running engines.^{1,2} Fluorescence imaging as well as ion-imaging techniques have added an extra dimension to photodissociation studies and to studies of (in)elastic and reactive scattering processes.^{3,4} In the field of quantum electronics, spatially resolved detection of metastable atoms is used to visualize minute photodeflection and atomic interference effects.

In this paper we report on 2D imaging of metastable molecules. First, direct time resolved (and spatially integrated) detection of laser prepared metastable CO molecules in a molecular beam is described. This detection technique is used to characterize the molecular beam in terms of parallel velocity distribution and rotational temperature. In contrast to similar time resolved measurements by Wodtke and co-workers⁵ we use a Micro-Channel Plate (MCP) to directly detect the metastable molecules, allowing for a straightforward extension of this technique to two dimensions. Direct 2D imaging of metastable CO molecules in the molecular beam is then used to measure the perpendicular velocity distribution of CO in the beam, and thereby completes the characterization of the molecular beam. A clear 2D visualization of the mass-focusing effect in binary CO/rare gas mixtures is given.

Direct 2D imaging of metastable CO molecules is also used to study the focusing performance of an electrostatic hexapole. Hexapoles are used throughout for state selection and orientation of polar symmetric top molecules using the first order Stark effect.⁶⁻⁸ Application of hexapoles in reaction dynamics and in molecular beam scattering experiments,⁹ in surface scattering experiments¹⁰ as well as in photodissociation studies^{11,12} has yielded a wealth of information on the steric effects in these processes. The opera-

tion characteristics of a hexapole are commonly determined via measurement of the focusing curve, i.e., via measurement of the (state-selective) molecular beam intensity integrated over a certain area as a function of the voltage applied to the hexapole rods.^{13,14} We here present measurements of the full 2D distributions of the metastable CO molecules in the beam after passage through a hexapole field as a function of the voltage applied to the hexapole rods. Structured 2D images demonstrate the dependence of the focusing characteristics on the magnitude of the Λ -doubling and show the effect of the deviations of the hexapole field in a hexapole consisting of cylindrical rods from the ideal hexapole field.

II. EXPERIMENTAL SET-UP

A schematic overview of the molecular beam machine is shown in Fig. 1. The machine is composed of two differentially pumped stainless steel vacuum chambers.

In the source chamber a pulsed valve (R.M. Jordan Co.) operating on the magnetic beam repulsion principle is mounted. The valve has a 0.35 mm diameter orifice and delivers gas pulses of 30 μ s duration at a repetition frequency of 10 Hz. A mixture of either 5% or 10% CO in a rare gas at a total backing gas pressure of 1.5 atm. is used for the supersonic expansion. About 2 cm downstream from the nozzle the jet-cooled ground state CO molecules are excited to the metastable $a^3\Pi(v'=0)$ state with pulsed 206 nm laser radiation. The molecular beam is subsequently collimated by a 0.8 mm diameter skimmer located 4 cm away from the nozzle, and enters the differentially pumped detection chamber.

In the detection chamber a 15 cm long electrostatic hexapole state selector is mounted, the entrance of which is 13 cm away from the laser excitation region. The 4 mm diameter cylindrical hexapole rods, located at the outside of a 8 mm diameter circle, provide an electric field that approximates the ideal hexapole field.^{14,15} A 1.2 mm diameter beam-stop can optionally be inserted 2 cm behind the end of the hexapole and can be adjusted via an UHV manipulator. At the end, the molecular beam impinges upon a 25 mm diameter MCP detector, used for the selective detection of the

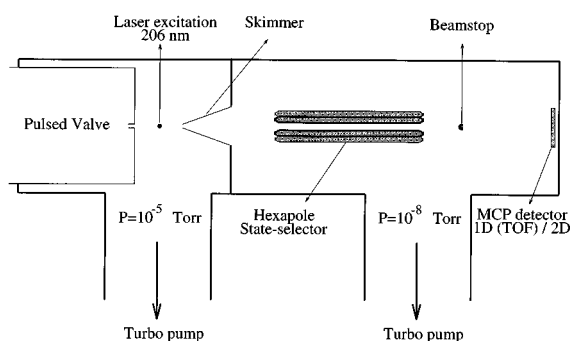


FIG. 1. Schematic overview of the molecular beam machine, composed of two turbo pumped vacuum chambers. The pulsed valve releases short gas pulses of CO diluted in a rare gas. Metastable $a^3\Pi(v'=0)$ CO molecules are prepared via pulsed laser excitation around 206 nm of jet-cooled ground state CO molecules, enter the differentially pumped detection chamber through the skimmer, pass through an electrostatic hexapole state-selector and finally impinge on a Micro-Channel Plate (MCP) detector where they are time and spatially resolved detected. Part of the beam can optionally be blocked by a beamstop.

metastable CO molecules. For the time-resolved (and spatially integrated) measurements the MCP detection stage is a double MCP with ns time resolution located 38 cm away from the excitation region. For the spatially resolved 2D imaging measurements a single MCP/phosphor screen (P20) detector located 49 cm away from the excitation region is used in combination with a CCD camera system.

The source chamber and the detection chamber are pumped by a 300 l/s and a 240 l/s turbo molecular pumping system, respectively, yielding background pressures of 1.5×10^{-5} Torr in the source chamber and below 10^{-8} Torr in the detection chamber under operating conditions.

The laser system used for quantum-state selective preparation of metastable CO molecules consists of a Nd:YAG laser pumped pulsed dye laser system (Spectra Physics, GCR 150/PDL-3 combination) operating on a DCM/Sulforhodamine 640 dye mixture that is optimized for producing 618 nm radiation. The output of the dye laser (95 mJ/pulse, 0.07 cm^{-1} bandwidth) is frequency tripled in a combination of a KDP and a BBO crystal, thus producing linearly polarized tunable 206 nm radiation with an energy of 1.5 mJ/pulse in a 0.2 cm^{-1} bandwidth. The laser light is focused by a 21 cm focal length lens into the molecular beam machine, intersecting the molecular beam perpendicularly. The light transmitted through the machine is focused back by a plano-concave mirror with a radius of curvature of 25 cm, thus doubling the number of metastable CO molecules.

For the time-resolved detection of the metastable CO molecules the double MCP detection stage is terminated with a 1 k Ω resistor to increase the detection sensitivity. The concomitant loss in time resolution (determined by the RC-time of the detection system) is unimportant on the time-scale of the actual time-of-flight (TOF) measurements. The TOF distributions are digitized and displayed on an oscilloscope with a 100 MHz sampling rate and a 10 bit vertical resolution (Lecroy 9430). From single shot TOF distributions it is deduced that the number of metastable molecules measured on

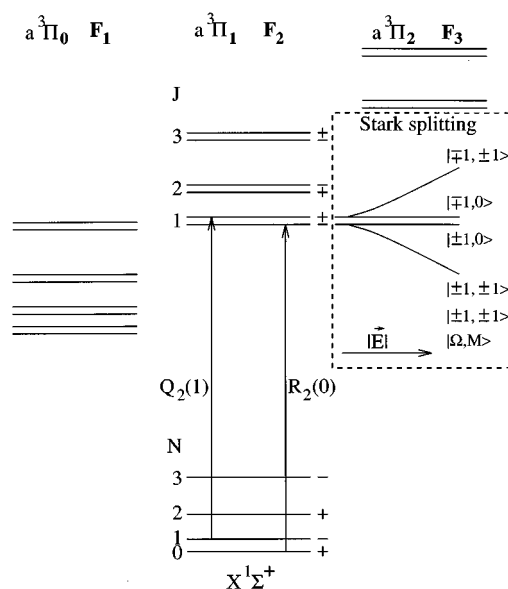


FIG. 2. Excitation scheme for the $a^3\Pi \leftarrow X^1\Sigma^+$ transition in CO. Quantum numbers and parity of the rotational levels are indicated. For low J values the dominant transitions are to the $\Omega=1$ component of the $a^3\Pi$ state, as indicated. The behavior of the Λ -doublet components of the $a^3\Pi_1$, $J=1$ level in an electric field is schematically indicated in the dashed box.

the detector is typically on the order of 10^3 – 10^4 per pulse. To improve the measurement statistics the TOF transients are averaged over 3000 shots. The averaged TOF transients are read into a 486-PC via a GPIB interface. Laser excitation spectra are recorded by measuring the time-integrated TOF signal as a function of the excitation laser frequency.

For the spatially resolved detection of the metastable CO molecules the combined MCP/phosphor screen detector is used. To suppress the background noise (e.g., from ion gauges) and to retain part of the time resolution the MCP is gated using a high voltage pulser. The phosphor screen is coupled to the outside of the vacuum machine by a fiber optical taper and imaged on a CCD chip with a 12 bit resolution and 384×288 pixels. The CCD chip is cooled to -15°C with a Peltier element to reduce the dark current. The CCD camera is interfaced to and controlled by a 486-PC. With this detection system (LaVision GmbH) the 2D spatial distribution of the CO molecules under various molecular beam conditions with and without applied hexapole fields have been visualized.

Triggering of valve, laser and detection system is regulated by a digital delay generator (DG535, Stanford Research Systems Inc.).

III. METASTABLE CO PRODUCTION AND DETECTION

Metastable CO molecules are produced via pulsed laser excitation of ground state CO molecules on the spin-forbidden $a^3\Pi(v'=0) \leftarrow X^1\Sigma^+(v''=0)$ transition (Cameron band) around 206 nm. Single rotational levels in the metastable state can be prepared. A detailed presentation of the excitation scheme is given in Fig. 2. In the $1^1\Sigma^+$ electronic ground state of CO, which is best described in the

Hund's case (b) approximation,¹⁶ the rotational structure is fully characterized by the quantum number N ($=J$) corresponding to the end-over-end rotation \bar{N} . The parity of the rotational levels in the electronic ground state is given by $(-1)^N$. The rotational structure in the $a^3\Pi$ state is characterized by the quantum number J , corresponding to the total angular momentum \bar{J} . For low J values, the $a^3\Pi$ state is best described in the Hund's case (a) approximation. In this approximation, three different rotational ladders belonging to the possible values of the quantum number Ω , in which $\bar{\Omega}$ is the projection of the total angular momentum \bar{J} on the internuclear axis, are distinguished. Each J level is split by the Λ -doubling in two components with opposite parity, as shown in the figure.

The spin-forbidden $a^3\Pi(v'=0) \leftarrow X^1\Sigma^+(v''=0)$ transition becomes weakly allowed due to spin-orbit interaction of the $A^1\Pi$ state with the $a^3\Pi$ state, i.e., due to the amount of $^1\Pi$ character in the $^3\Pi$ state. The selection rules are therefore identical to those of a $^1\Pi \leftarrow ^1\Sigma^+$ transition. In the pure Hund's case (a) description this implies that only transitions to the $\Omega=1$ multiplet component of the $a^3\Pi$ state are allowed. For higher J values there is a considerable amount of mixing of the various multiplet components in the triplet state,¹⁷ and excitation is no longer restricted to the $\Omega=1$ component only. The validity of this model¹⁸ has been experimentally verified in previous studies.^{5,19,20} The radiative lifetime of the metastable CO molecules is several ms, and is strongly J dependent. The prominent transitions used in our experiments are indicated in Fig. 2 using the conventional notation $\Delta J_{F_{\text{final}}}(N'')$,¹⁶ where F_{final} is F_1 , F_2 , and F_3 for Ω is 0, 1, and 2, respectively.

In the presence of an external electric field, as the electrostatic hexapole field, the $(2J+1)M$ degeneracy of each J level, where M is the projection of \bar{J} in the direction of the electric field, is lifted. In the $X^1\Sigma^+$ state only a second order Stark effect exists, yielding negligible (MHz) splittings in the electric fields applied in the hexapole. In the metastable $a^3\Pi_1$ state there is a first-order Stark effect and with a dipole moment of 1.37 D^{21} Stark splittings on the order of a GHz occur in the hexapole field under our operating conditions. The behavior of the Λ -doublet components for the $J=1$ level in the $a^3\Pi_1$ state in an electric field²¹ is schematically indicated in the dashed box in Fig. 2. In zero electric field the splitting of these Λ -doublet components is 394 MHz. With the hexapole state selector (Ω, J, M) levels with a positive Stark effect, i.e., levels that increase in energy with increasing electric field strength, can be focused and a (Ω, J, M) state selected and oriented molecular beam can be produced. The $M=0$ levels cannot be deflected by a hexapole field at all whereas states with a negative Stark effect can only be defocused.

In the experiments reported here the laser preparation of the metastable CO molecules takes place in zero electric field so there is no M selection in the excitation process, and M state selection only takes place afterward in the hexapole field. An alternative approach for the production of a beam of state-selected and oriented metastable CO molecules is to induce the $a^3\Pi(v'=0) \leftarrow X^1\Sigma^+(v''=0)$ transition in a static electric field with a laser that has a bandwidth that is

narrow enough that individual $M' \leftarrow M''$ transitions can be resolved.²² As will be shown explicitly below, however, hexapole state selection and focusing has the advantage that it permits a complete discrimination against ground state CO molecules and against the rare gas carrier atoms. A truly pure beam of state-selected and oriented metastable CO molecules can thus be produced.

The electronically excited metastable CO molecules are detected via the ejection of electrons from a metal when the metastable molecules impinge on this metal. Various studies have been performed on the ejection of electrons from metals by impact of atomic (metastable) ions.^{23,24} An early theoretical description of these processes has been given by Hagstrum in 1954.²⁵ Auger de-excitation processes of metastable neutral atoms have also been studied and these studies have led to the development of metastable atom de-excitation spectroscopy as a surface spectroscopic technique.²⁶

Generally, when a metastable molecule collides with a metal surface the metastable molecule can be de-excited via two mechanisms. The first mechanism is resonant ionization of the excited molecule followed by Auger neutralization. The second mechanism is direct Auger de-excitation of the metastable molecule. Both processes eject Auger electrons but can be distinguished by the different kinetic energy distributions of the ejected electrons. The resonant ionization process is a one-electron process that takes place when the metastable is still relatively far away from the surface, a process much faster than the two-electron Auger de-excitation process. The resonant ionization process can only occur, however, when the effective ionization potential of the metastable molecule is less than the workfunction of the metal, i.e. only if the energy of the metastable level is above the Fermi level of the metal. The 6 eV internal energy of the metastable CO $a^3\Pi$ molecules is sufficient to eject Auger electrons from nearly any metal. As there is still 8 eV needed to ionize the metastable molecules, however, all these electrons are produced in a direct Auger de-excitation process only. This latter process is schematically indicated in Fig. 3, for a metastable CO molecule at a distance S from a metal surface with a work function Φ and a Fermi energy W . An electron from the conduction band of the metal is used to de-excite the metastable molecule and the energy gained in this process can be used to let an electron escape from the metal/molecule system with a kinetic energy $E_k(e^-)$ equal to the excess energy.

When a metastable CO molecule strikes the surface of a MCP detector the aforementioned Auger de-excitation process takes place as well. The produced Auger electrons are multiplied by the MCP and single emitted Auger electrons can thus be detected. The work function of the MCP detectors we used is approximately 5 eV and metastable CO $a^3\Pi(v'=0)$ molecules can be time and spatially resolved detected with an estimated efficiency of a few percent.

IV. RESULTS AND DISCUSSION

A. Molecular beam characterization

Time resolved measurements are performed to determine the velocity distribution of ground state CO molecules in a

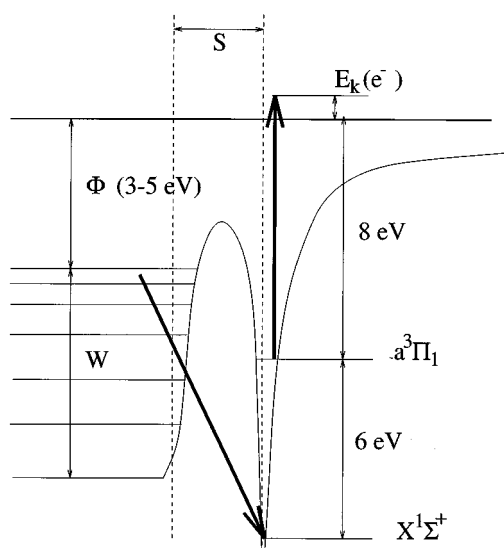


FIG. 3. Energy level structure of a metastable CO molecule at a distance S from a metal surface (work function Φ , Fermi energy W). Metastable CO molecules are detected via the electrons that are ejected according to the indicated Auger de-excitation process.

well-defined quantum state as well as to determine the rotational temperature of the supersonically expanded molecular beam. The parallel velocity distribution $f(v_{\parallel})$ for a specific rotational level in the $X^1\Sigma^+(v''=0)$ state is directly deduced from the measured time-of-flight (TOF) distribution of metastable CO molecules that are prepared out of this specific rotational level. In Fig. 4 the measured TOF distributions for 5% CO expanding in He, Ne, Ar, Kr, and Xe are shown. These TOF distributions are measured after excitation on the $R_2(0)$ transition, thus monitoring the TOF of CO molecules in the $X^1\Sigma^+(v''=0, N''=0)$ state. On the horizontal axis the time-of-flight for the 38 cm path from the laser excitation region to the detector is indicated. Vertically the signal intensity is shown, where more metastable molecules lead to a more negative signal.

The observed TOF distributions can be fit to a Gaussian velocity distribution²⁷

$$f(v_{\parallel}) = \left(\frac{m}{2\pi kT_{\parallel}} \right)^{1/2} e^{-S_{\parallel}^2 [1 - (v_{\parallel}/\bar{v}_{\parallel})]^2} \quad (1)$$

in which \bar{v}_{\parallel} is the average parallel velocity, m is the mass of the carrier gas, k is Boltzmann's constant and T_{\parallel} is the parallel translational temperature, a parameter determined by the width of the velocity distribution. The parallel speed ratio S_{\parallel} is related to T_{\parallel} via

$$S_{\parallel} = \frac{\bar{v}_{\parallel}}{\left(\frac{2kT_{\parallel}}{m} \right)^{1/2}}. \quad (2)$$

The resulting parameters of the fit (\bar{v}_{\parallel} , T_{\parallel} and S_{\parallel}) are tabulated in Table I for the various TOF distributions displayed in Fig. 4. The observed TOF distributions are accurately described by this velocity distribution function, and a more detailed description²⁸ is therefore omitted. The experimen-

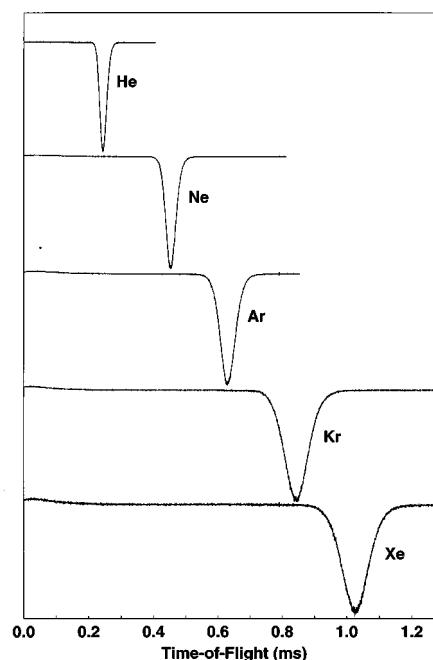


FIG. 4. Measured time-of-flight (TOF) distributions for 5% CO expanding in He, Ne, Ar, Kr, and Xe. The TOF distributions are measured after excitation on the $R_2(0)$ transition, thus monitoring CO molecules in the $X^1\Sigma^+(v''=0, N''=0)$ ground state. On the horizontal axis the time-of-flight for the 38 cm path from the laser excitation region to the detector is indicated.

tally observed average parallel velocities correspond to effective buffer-gas temperatures that are clearly above room temperature (except for He) probably due to heating of the gas mixture by the intense current pulses used for operating the valve.

The rotational temperature of the CO molecules in the molecular beam is determined from excitation spectra measured for all the gas mixtures used in the TOF experiments. An example of an excitation spectrum is given in Fig. 5 for a mixture of 10% CO in Ar, as it has a slightly better signal to noise ratio than the 5% CO/rare gas mixtures. On the horizontal axis the absolute laser frequency (in cm^{-1}) is indicated while vertically the time-integrated TOF-signal intensity is shown. The upper trace shows the measured excitation spectrum in the region of the most intense Q_2 and R_2 lines of ^{12}CO . Several lines of the ^{13}CO isotope, present in the gas mixture at a natural abundance of 1.1%, are indicated in the

TABLE I. Parameters characterizing the molecular beam for various binary 5% CO/rare gas mixtures. The average parallel velocity (\bar{v}_{\parallel}), the parallel translational temperature (T_{\parallel}) and the associated parallel speed ratio (S_{\parallel}), the FWHM of the perpendicular velocity distribution (Δv_{\perp}) and the rotational temperature (T_{rot}) are given.

Carrier gas	\bar{v}_{\parallel} (m/s)	T_{\parallel} (K)	S_{\parallel}	Δv_{\perp} (m/s)	T_{rot} (K)
He	1560±10	2.2±0.2	16.0±1.2		15.0±2.0
Ne	840±5	2.1±0.2	20.3±1.5	16.3±0.9	4.7±0.3
Ar	600±4	2.4±0.2	19.1±1.4	16.4±1.2	5.2±0.3
Kr	450±3	3.9±0.3	16.1±1.2		3.7±0.3
Xe	370±2	3.5±0.3	17.4±1.3	17.6±1.6	3.3±0.3

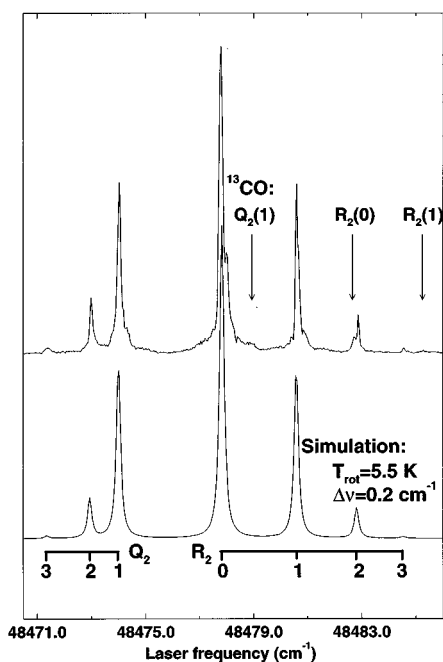


FIG. 5. Upper trace: Excitation spectrum of a mixture of 10% CO in Ar in the region of the most intense Q_2 and R_2 lines of ^{12}CO . The time-integrated TOF-signal intensity is plotted against the absolute laser frequency. The strongest lines of the ^{13}CO isotope, present at a natural abundance of 1.1%, are indicated in the spectrum by vertical arrows. Lower trace: Best fitting simulated spectrum assuming a Lorentzian laser profile with a FWHM of $\Delta\nu=0.2\text{ cm}^{-1}$. A rotational temperature $T_{\text{rot}}=5.5\text{ K}$ is found.

experimental spectrum by vertical arrows. The lower trace shows the corresponding simulated spectrum of ^{12}CO , using the known transition frequencies¹⁷ and relative transition strengths¹⁸ and using a Boltzmann distribution for the population of the rotational levels in the electronic and vibrational ground state. The spectrum is best simulated with a rotational temperature $T_{\text{rot}}=5.5\text{ K}$ and a Lorentzian laser profile with a full width at half maximum (FWHM) of 0.2 cm^{-1} . Since the residual Doppler width in the molecular beam is about two orders of magnitude smaller than the laser bandwidth, the line shape in the excitation spectra is solely determined by the laser. The rotational temperatures found via this procedure for all the gas mixtures used in the TOF experiments are given in the last column of Table I.

To determine the velocity distribution of the CO molecules perpendicular to the molecular beam axis, spatially resolved detection of the laser prepared metastable CO molecules is performed. Two-dimensional images showing the spatial distribution of CO in the molecular beam in a false color representation are given in Fig. 6 for mixtures of 5% CO in He, Ne, Ar and Xe. To record these 2D images the MCP detector is gated to integrate over only the most intense part of the TOF signal intensity; typically a gate with a width of 10% of the mean arrival time is used. The images are averaged over 10^4 laser shots with the laser resonant on the $R_2(0)$ transition while a background image, recorded without laser excitation, is subtracted. The size of the images corresponds to a detector area of $26.9\text{ mm}\times 23.3\text{ mm}$ (300×260 pixels on the CCD chip). The color table next to the images

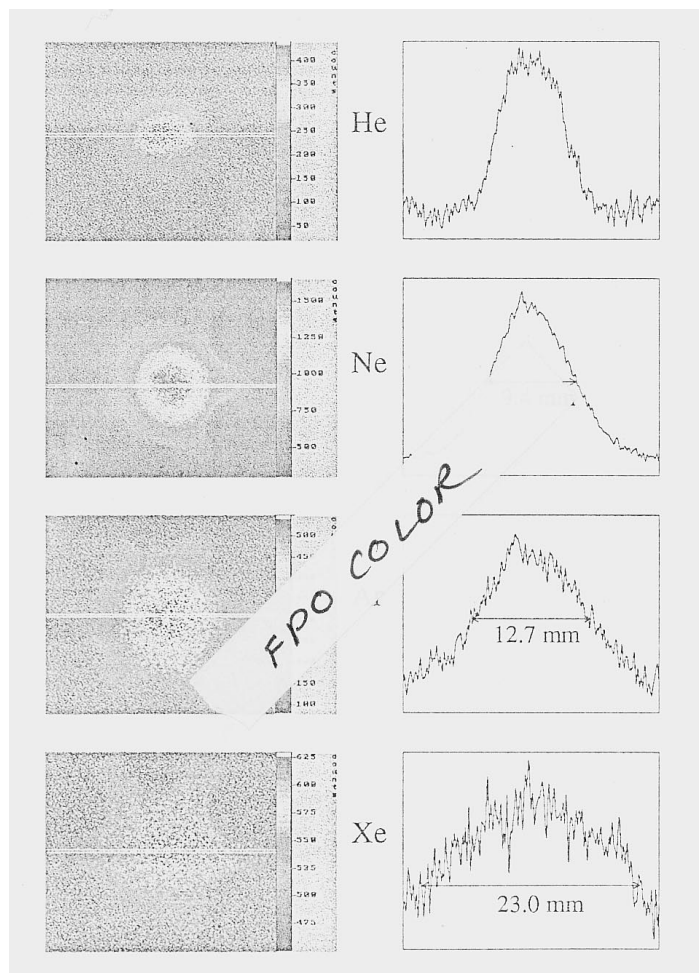


FIG. 6. Two-dimensional images ($26.9\text{ mm}\times 23.3\text{ mm}$) showing the spatial distribution of CO in the molecular beam for mixtures of 5% CO in He, Ne, Ar and Xe. The color associated with a certain pixel intensity on the detector is indicated next to the images. In most of the 2D-images the ‘shadow’ of the hexapole-rods is clearly visible. The series of images demonstrates the mass-focusing effect by which in a molecular beam of a binary mixture the heavier species is concentrated on the molecular beam axis. On the right-hand side the horizontal intensity profiles of the corresponding 2D images are shown, averaged over the 6 horizontal lines around the center of the image, indicated by the white lines in the images. The FWHM of the spot on the detector (in mm) is indicated for those profiles that can be fit using a simple Gaussian perpendicular velocity distribution.

indicates the color associated with a certain pixel intensity on the detector. The images are smoothed by Fourier filtering techniques to eliminate the high frequency noise and are corrected for a somewhat higher sensitivity in a small central spot, caused by local cleaning of the MCP detector in the hexapole focus.

In most of the 2D images of Fig. 6 the “shadow” of the hexapole rods is clearly visible. The actual distance between two opposite hexapole rods is 8.0 mm , which appears as an enlarged $14.4 \pm 0.3\text{ mm}$ distance on the detector due to the experimental geometry. It is evident from these images that the molecular beam is slightly misaligned from the center of the hexapole axis. The series of images displayed in this figure demonstrates the mass-focusing effect, i.e., the effect that in a molecular beam of a binary mixture the heavier species is concentrated on the molecular beam axis.²⁷ In this

series of images it is seen that the width of the CO distribution in the beam increases with increasing mass of the carrier gas; for the lightest carrier gas, He, the “shadow” of the hexapole rods is not even visible. On the right hand side of the figure the horizontal intensity profiles of the corresponding 2D images are shown. These profiles are averaged over the 6 horizontal lines around the center of the image, indicated by the white lines in the images. Except for the He image, the shape of the profiles is accurately described by a Gaussian curve, and the resulting FWHM of the best-fitting Gaussian curve is indicated (in mm) in the figure. The corresponding FWHM of the perpendicular Gaussian velocity distribution, Δv_{\perp} , is given in Table I.

The observed mass-focusing effect can be explained in a rather simple model.²⁷ As the collisions between CO molecules and carrier gas atoms in the expansion are essentially along the molecular beam axis the velocity of the CO molecules in this direction adapts to the velocity of the carrier gas, as is demonstrated in the TOF distributions shown in Fig. 4. The velocity distribution perpendicular to the molecular beam axis is mainly determined by the velocity of the CO molecule itself, however, implying a perpendicular velocity distribution that is independent of the carrier gas, as is evident from the values of Δv_{\perp} given in Table I. This then results in a spatial width of the CO distribution in the molecular beam that scales linearly with $1/\bar{v}_{\parallel}$, as is indeed observed for CO seeded in Ne, Ar, and Xe.

In the interpretation of the experimental observations it is assumed that no disturbing collisions take place between the laser excitation region and the detector. For the heavy carrier gases, possible disturbing effects related to shock waves in the source chamber can be circumvented by exciting CO molecules in the front part of the short gas pulse. For Ne, for instance, the gas pulse has a length of around 2.5 cm, which is shorter than the skimmer length, so shock waves can only build up after passage of the excited molecules through the skimmer. In the faster He beam, however, shock waves can not be completely avoided which might be the explanation for the relatively high rotational temperature, for the lower than expected parallel velocity and for the deviation of the perpendicular velocity distribution from a Gaussian curve.

B. Hexapole focusing

Prior to discussing the experimental observations, a description of the trajectories of metastable CO molecules through a hexapole field is given. The electrostatic potential in an *ideal* hexapole is given by⁶

$$V = \frac{V_0}{2} \left(\frac{r}{r_0} \right)^3 \cos 3\phi, \quad (3)$$

where r and ϕ are the cylindrical coordinates (the z axis coincides with the axis of the hexapole, $z=0$ at the beginning of the hexapole), V_0 is the voltage difference between neighboring rods and r_0 is the inner radius of the hexapole. The azimuthal angle ϕ is zero in the direction of the center of one of the hexapole rods. The electric field \vec{E} derived from this potential is

$$\vec{E} = \left[-3 \frac{V_0}{2} \left(\frac{r^2}{r_0^3} \right) \cos 3\phi, 3 \frac{V_0}{2} \left(\frac{r^2}{r_0^3} \right) \sin 3\phi, 0 \right] \quad (4)$$

in the (r, ϕ, z) cylindrical coordinates. The Stark splitting of the energy levels in the $a^3\Pi_{\Omega}$ state only depends on the absolute value of the electric field $|\vec{E}|$ which, in the ideal hexapole, is independent of ϕ . The magnitude of the Stark shift of a Λ -doublet level ΔW_{Stark} relative to the zero-field energetic center of the Λ -doublet components is given by²¹

$$\Delta W_{\text{Stark}} = \left(\left(\frac{\Lambda}{2} \right)^2 + (E_{\text{Stark}})^2 \right)^{1/2}. \quad (5)$$

In this expression Λ is the magnitude of the Λ -doubling and E_{Stark} is the first order Stark effect in an electric field $|\vec{E}|$, given by

$$E_{\text{Stark}} = -\mu_{\text{el}} |\vec{E}| \frac{M\Omega}{J(J+1)} = -\mu_{\text{el}} 3 \frac{V_0}{2} \left(\frac{r^2}{r_0^3} \right) \frac{M\Omega}{J(J+1)} \quad (6)$$

containing the electric dipole moment μ_{el} , the absolute value of the electric field and the quantum numbers Ω , J and M . The force exerted by a hexapole field on the CO molecules is determined by the gradient of ΔW_{Stark} , resulting in the equation of motion

$$m_{\text{CO}} v_{\parallel}^2 \frac{d^2 r}{dz^2} = - \frac{|E_{\text{Stark}}|}{\Delta W_{\text{Stark}}} \frac{dE_{\text{Stark}}}{dr} \quad (7)$$

in which m_{CO} is the mass of the CO molecule. It should be noted that there is only a radial force present in the ideal hexapole.

In the high electric field limit, ΔW_{Stark} can be approximated by $|E_{\text{Stark}}|$, resulting in an equation of motion according to which the CO molecules describe a sinusoidal path in the hexapole field. Although this high electric field approximation is commonly made, it is, however, not valid for the given experimental situation. The electric field around the center of the hexapole is rather low resulting in a Stark energy comparable to the Λ -doublet splitting, causing a deviation from a sinusoidal path of the CO molecules.^{8,15}

It has already been mentioned, and it is clear from the above equations, that only metastable CO molecules with a positive Stark effect (the upper Λ -doublet component with $M\Omega < 0$) can be focused, while a negative Stark effect (the lower Λ -doublet component, with $M\Omega > 0$) leads to defocusing of the molecules. From the excitation scheme in Fig. 2 it follows that Q_2 lines have to be used to produce $a^3\Pi_1$ metastable CO molecules that can be focused by the hexapole. The $M=0$ $a^3\Pi_1$ states and the ground state CO molecules (where $\Lambda=\Omega=0$) can not be deflected at all. This implies that the number of metastable CO molecules can be enormously enlarged relative to the number of ground state CO molecules by using the hexapole and that single $a^3\Pi$ (Ω, J, M) quantum states can be selected.

In Fig. 7, two-dimensional images of the distribution of the laser prepared metastable CO molecules in the molecular beam are shown as a function of the voltage on the hexapole-rods. Laser excitation is performed on the $Q_2(1)$ transition in a mixture of 5% CO in Kr carrier gas. The size of the displayed images corresponds to a 12.6 mm \times 12.6 mm area on the detector (140 \times 140 pixels on the CCD chip; smaller than

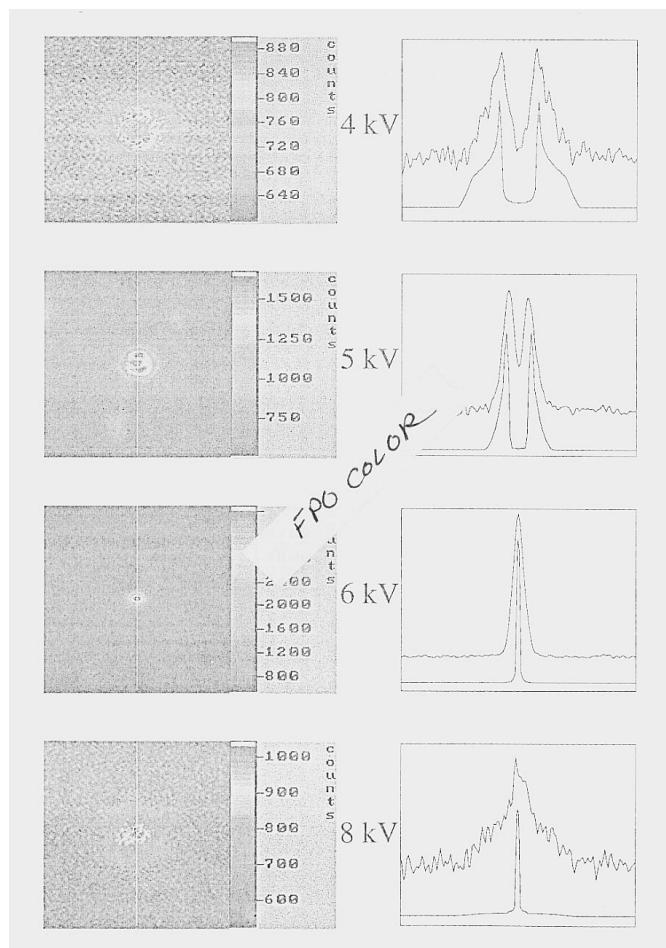


FIG. 7. Two-dimensional images ($12.6 \text{ mm} \times 12.6 \text{ mm}$) of the distribution of metastable CO molecules [5% CO in Kr; $Q_2(1)$ excitation] in the molecular beam as a function of the voltage on the hexapole rods. The series of images shows a clear ring pattern due to the Λ -doubling in the under-focused situation (4 kV; 5 kV), a sharp spatial focus at a hexapole voltage of 6 kV and again a broader distribution in the over-focused situation (8 kV). Attention is drawn to the apparent rotation of the sixfold symmetry in the 2D-images over 30° in going from the under-focused to the over-focused situation, due to the ϕ dependence of the radial force acting on the metastable CO molecules. Vertical profiles taken along the white line in the 2D images are shown as the upper trace in the plots next to the images. The lower trace in each of these plots shows the profiles as calculated using the (ideal) hexapole focusing theory.

in the mass-focusing images). The images are averaged over 10^4 laser shots with a background subtracted. To prevent saturation effects on the CCD chip, the 6 kV focusing image has been averaged over 5000 shots only. The images are smoothed by Fourier filtering techniques and corrected for the increased sensitivity at the hexapole focus. Separate color tables indicate the color associated with a certain pixel intensity for each image. The series of images shows a clear ring-pattern in the under-focused situation (4 kV; 5 kV), a sharp spatial focus at a hexapole voltage of 6 kV and again a broader distribution in the over-focused situation (8 kV). Attention is drawn to the apparent rotation of the sixfold symmetry in the 2D images over 30° in going from the under-focused to the over-focused situation. Vertical profiles taken along the white line in the 2D images are shown as the upper trace in the plots next to the images. The lower trace in each

of these plots shows the profiles as calculated using the aforementioned hexapole focusing theory. To obtain these calculated profiles, the equation of motion (7) is solved numerically. All input parameters for this calculation are known experimentally so there are no adjustable parameters. The geometry of the molecular beam machine, the voltage applied to the hexapole rods, the gating on the MCP detector, the parallel velocity distribution as derived from the TOF measurements, the perpendicular velocity distribution as derived from the (unfocused) 2D images, the quantum numbers of the laser prepared metastable levels as well as the magnitude of the Λ -doubling are used as input in the calculation of the profiles. The hexapole field is assumed to switch on and off abruptly at the beginning and end of the hexapole, respectively. For the under-focused situation the calculated profiles match the experimental ones rather well. The width of the calculated focus at 6 kV is smaller than the experimentally observed width (0.8 mm FWHM) and the calculated profile in the over-focused situation does not agree that well with the observed profile which we attribute to deviations of our hexapole field from an ideal hexapole field, as will be discussed below. The slight misalignment of the molecular beam with the axis of the hexapole will also give a minor deviation (image distortion due to “spherical” aberration).

The observed ring-pattern in the under-focused situation, which is quantitatively reproduced in the calculations, is caused by the magnitude of the Λ -doubling; the diameter of the ring at a certain hexapole voltage is a direct measure for the magnitude of the Λ -doubling. In the absence of Λ -doubling (or generally, if the high field approximation is valid), all molecules entering the hexapole with the same velocity but under various angles with respect to the hexapole axis can be focused in the same point. The presence of the Λ -doubling decreases the force exerted on the metastable molecules that are near to the hexapole-axis relative to the force that would be present in the high electric field approximation, whereas the high electric field approximation is valid for metastable molecules that are further away from the hexapole axis. This leads to a focusing of the latter molecules at a lower voltage than needed for focusing the metastable molecules that are near to the hexapole axis, thus explaining the observed rings.

A more accurate description of the electric field as well as of the equations of motion of dipolar molecules in a hexapole consisting of cylindrical rods has been given by Vonbun.¹⁵ It follows that the gradient of the electric field in the radial direction inside such a hexapole has a ϕ -dependence, that becomes increasingly important for distances further away from the hexapole axis. This ϕ -dependence results in a radial force that is maximum for molecules that travel in the direction of the center of a hexapole rod and minimum for molecules that travel in the direction in between hexapole rods. In the hexapole used in this study the ratio of the maximum to the minimum value of $d|\vec{E}|/dr$ is calculated to be around 1.04 at a distance of $0.5 r_0$, increasing to almost a factor 2 at a distance of $0.8 r_0$ from the hexapole axis. This ϕ dependence of the radial force is held responsible for the already mentioned rotation

of the sixfold symmetry in the series of 2D images.

In the 2D images taken in the under-focused situation at 4 kV and 5 kV it is seen that the sixfold symmetry is such that the image is somewhat less extended in the direction of the hexapole rods. This effect can be explained by the previously shown “shadowing” effect of the hexapole rods (Fig. 6), i.e., by viewing the under-focused 2D images as (ϕ independently) compressed reproductions of the unfocused 2D images shown in Fig. 6. Alternatively, this effect can be explained by (or at least will be enhanced by) the ϕ dependence of the radial force acting on the metastable CO molecules. The ϕ dependence of the radial force is the only explanation of the apparent rotation of the image in the over-focused (8 kV) situation, however; molecules travelling in the direction of one of the hexapole rods will feel the strongest radial force and will therefore be deflected most efficiently and be bent away most strongly from the molecular beam axis in the over-focusing situation. A yet alternative explanation would invoke the presence of a velocity component in the ϕ -direction induced either by the force component in this direction which is present in our nonideal hexapole field¹⁵ or by the misalignment of the molecular beam on the hexapole axis. This explanation can be discarded, however, as the magnitude of the resulting rotation should change with the hexapole voltage and the parallel velocity of the CO molecules, something that has not been observed.

In the near future this molecular beam machine will be coupled to an UHV system to study the interaction between the metastable CO molecules and a variety of well-defined metal surfaces. To avoid interfering effects due to either ground state CO molecules or due to carrier gas atoms a truly pure beam of state-selected metastable CO molecules is needed. To obtain such a pure beam a beamstop is centered on the molecular beam axis. In the upper image of Fig. 8 the distribution of metastable CO molecules in the molecular beam (5% CO in Ar), with no voltage applied to the hexapole rods, is shown. Apart from the “shadow” of the hexapole rods, the “shadow” of the 1.2 mm diameter beamstop as well as of the 0.1 mm diameter wire to which this beamstop is attached can be recognized. As is explicitly shown in the lower image of Fig. 8, the metastable CO molecules can be bent around this beamstop and focused in a spot centered in the “shadow” of the beamstop. A diaphragm with the appropriate dimensions placed in the focal plane will transmit only the pure state-selected metastable CO beam.

V. CONCLUSIONS

Metastable $a^3\Pi$ CO molecules can be state-selectively prepared and sensitively detected on a MCP detector via Auger de-excitation making both time and spatially resolved measurements possible. The combination of these techniques is used for a straightforward characterization of a molecular beam, and parallel and perpendicular velocity distributions as well as rotational temperatures are determined. A direct 2D demonstration of the mass-focusing effect in a binary gas mixture is given.

Two-dimensional imaging of the spatial distribution of the metastable $a^3\Pi$ CO molecules in the beam after passage through a hexapole field is used to study hexapole focusing

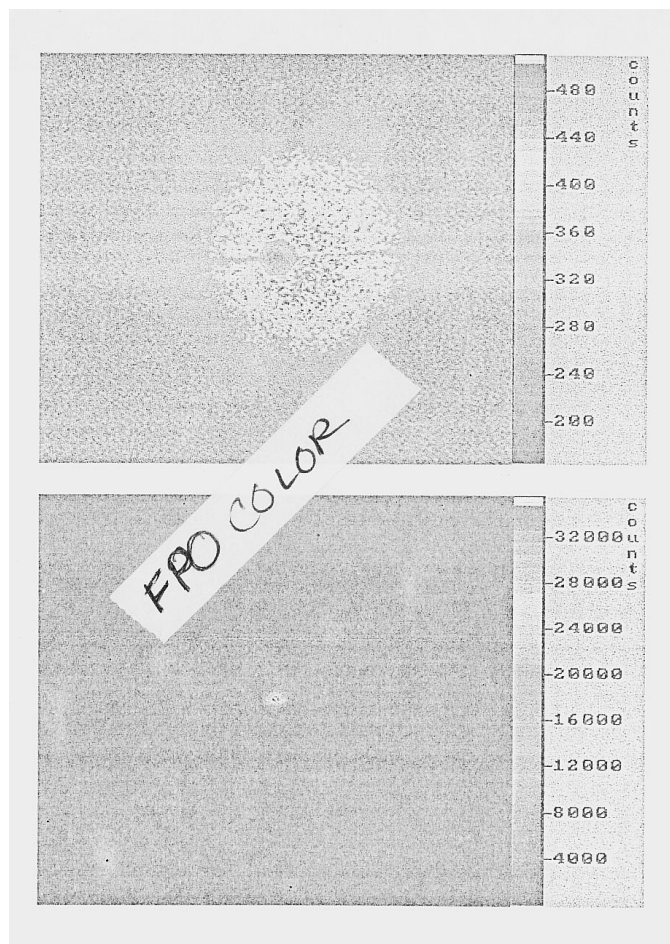


FIG. 8. Upper image: Distribution of metastable CO molecules in the beam (5% CO in Ar), with no voltage applied to the hexapole rods. Apart from the “shadow” of the hexapole rods, the “shadow” of the beamstop assembly can be recognized. Lower image: The metastable CO molecules are bent around the beamstop and focused (12 kV) in a spot centered in its “shadow.”

performance. Structured 2D images demonstrate the dependence of the focusing characteristics on the magnitude of the Λ -doubling and on the angular dependence of the focusing force in a hexapole consisting of cylindrical rods.

Laser preparation of quantum-state selected metastable molecules in combination with time and spatially resolved detection of the metastable species holds great promise in fields like, for instance, photo-dissociation dynamics and reactive and (in)elastic scattering. Compared to ion-imaging techniques, metastable imaging has the advantage that problems related to space-charge effects and related to the presence of spurious electric and/or magnetic fields are avoided.

ACKNOWLEDGMENTS

We thank Professor Dr. D. H. Parker and Dr. J. J. ter Meulen for useful discussions and helpful suggestions and C. A. Sikkens, J. G. H. Hermsen, and C. A. Timmer for technical support. We acknowledge LaVision GmbH (Göttingen, Germany) for lending us the 2D imaging detector as well as for software support.

- ¹R. K. Hanson, J. M. Seitzman, and P. H. Paul, *Appl. Phys. B.* **50**, 441 (1990).
- ²P. Andresen, G. Meijer, H. Schlüter, H. Voges, A. Koch, W. Hentschel, W. Oppermann, and E. Rothe, *Appl. Opt.* **29**, 2392 (1990).
- ³D. W. Chandler and P. L. Houston, *J. Chem. Phys.* **87**, 1445 (1987).
- ⁴T. N. Kitsopoulos, M. A. Buntine, D. P. Baldwin, R. N. Zare, and D. W. Chandler, *Science* **260**, 1605 (1993).
- ⁵J. M. Price, A. Ludviksson, M. Nooney, M. Xu, R. M. Martin, and A. M. Wodtke, *J. Chem. Phys.* **96**, 1854 (1992).
- ⁶K. H. Kramer and R. B. Bernstein, *J. Chem. Phys.* **42**, 767 (1965).
- ⁷*Atomic and Molecular Beam Methods*, edited by G. Soles Vol. I. (Oxford University Press, London/New York, 1988).
- ⁸J. Reuss, see Ref. 7, pp. 276–292.
- ⁹S. Stolte, see Ref. 7, pp. 631–652.
- ¹⁰E. W. Kuipers, M. G. Tenner, A. W. Kleyn and S. Stolte, *Phys. Rev. Lett.* **62**, 2152 (1989).
- ¹¹S. R. Gandhi and R. B. Bernstein, *J. Chem. Phys.* **88**, 1472 (1988).
- ¹²J. W. G. Mastenbroek, C. A. Taatjes, K. Nauta, M. H. M. Janssen and S. Stolte, *Nature* (submitted).
- ¹³S. R. Gandhi, T. J. Curtiss, Q. Xu, S. E. Choi, and R. B. Bernstein, *Chem. Phys. Lett.* **132**, 6 (1986).
- ¹⁴F. Harren, D. H. Parker and S. Stolte, *Comments At. Mol. Phys.* **26**, 109 (1991).
- ¹⁵F. O. Vonbun, *J. Appl. Phys.* **29**, 632 (1958).
- ¹⁶G. Herzberg, *Spectra of Diatomic Molecules*, 2nd ed. (Van Nostrand Reinhold, New York, 1950).
- ¹⁷R. W. Field, S. G. Tilford, R. A. Howard and J. D. Simmons, *J. Mol. Spectrosc.* **44**, 347 (1972).
- ¹⁸T. C. James, *J. Chem. Phys.* **55**, 4118 (1971).
- ¹⁹G. Meijer, A. M. Wodtke, H. Voges, H. Schlüter and P. and Andresen, *J. Chem. Phys.* **89**, 2588 (1988).
- ²⁰R. T. Jongma, M. G. H. Boogaarts, and G. Meijer, *J. Mol. Spectrosc.* **165**, 303 (1994).
- ²¹R. C. Stern, R. H. Gammon, M. E. Lesk, R. S. Freund, and W. A. Klemperer, *J. Chem. Phys.* **52**, 3467 (1970).
- ²²M. Drabbels, S. Stolte, and G. Meijer, *Chem. Phys. Lett.* **200**, 108 (1992).
- ²³H. D. Hagstrum, *Phys. Rev.* **96**, 325 (1954).
- ²⁴H. Brenten, H. Müller, K. H. Knorr, D. Kruse, H. Schall, and V. Kemper, *Surf. Sci.* **243**, 309 (1991).
- ²⁵H.D. Hagstrum, *Phys. Rev.* **96**, 336 (1954).
- ²⁶B. Woratschek, W. Sesselmann, J. Küppers, G. Ertl, and H. Haberland, *Phys. Rev. Lett.* **55**, 1231 (1985).
- ²⁷D. R. Miller, (1988), see Ref. 7 pp. 14–53.
- ²⁸H. C. W. Beijerinck, G. H. Kaashoek, J. P. M. Beijers, and M. J. Verheijen, *Physica* **121**, 425 (1983).